# Three-Dimensional Subsurface Analysis of Electromagnetic Scattering from Penetrable/PEC Objects Buried Under Rough Surfaces: Use of the Steepest Descent Fast Multipole Method

Magda El-Shenawee, *Member, IEEE*, Carey Rappaport, *Senior Member, IEEE*, Eric L. Miller, *Member, IEEE*, and Michael B. Silevitch

***Abstract*—The electromagnetic scattering from a three-dimensional (3-D) shallow object buried under a two-dimensional (2-D) random rough dielectric surface is analyzed in this work. The buried object can be a perfect electric conductor (PEC) or can be a penetrable dielectric with size and burial depth comparable to the free-space wavelength. The random rough ground surface is characterized with Gaussian statistics for surface height and for surface autocorrelation function. The Poggio, Miller, Chang, Harrington, and Wu (PMCHW) integral equations are implemented and extended in this work. The integral equation-based steepest descent fast multipole method (SDFMM), that was originally developed at UIUC, has been used and the computer code based on this algorithm has been successfully modified to handle the current application. The significant potential of the SDFMM code is that it calculates the unknown moment method surface electric and magnetic currents on the scatterer in a dramatically fast, efficient, and accurate manner. Interactions between the rough surface interface and the buried object are fully taken into account with this new formulation. Ten incident Gaussian beams with the same elevation angle and different azimuth angles are generated for excitation as one possible way of having multiple views of a given target.**

**The scattered electric fields due to these ten incident beams are calculated in the near zone and their complex vector average over the multiple views is computed. The target signature is obtained by subtracting the electric fields scattered from the rough ground only from those scattered from the ground with the buried anti-personnel mine. Significant polarization dependency is observed for the PEC object signature compared with that of the penetrable object, which can be used in target discrimination. Moreover, fields scattered above the rough ground experience significantly more distortion than fields transmitted into the ground.**

***Index Terms*—Buried-target, computational electromagnetics, fast multipole method (FMM), mine detection, rough surface scattering.**

## I. Introduction

SUBSURFACE sensing of buried electromagnetically penetrable objects under random rough surfaces has many important applications, such as detection of mines, underground water, buried hazardous environmental waste, and underground petroleum. Modeling the wave scattering is essential for efficient sensor design and for inverse scattering and target reconstruction processing. Of particular interest here is the topic of anti-personnel landmine detection, as shown schematically in Fig. 1. The analysis of scattering and transmission of the electromagnetic waves in the presence of a random rough dielectric interface and in the near field of the sensing systems is a crucial step for subsurface object detection problems in general and landmine remediation applications in particular. Generally, this fully three-dimensional (3-D) problem must be treated numerically. However, the calculation of the required fields using conventional techniques (e.g., moment method, finite elements, or finite differences) is a computationally intensive undertaking especially for large dielectric constant soil. The computational complexity of the problem dramatically increases upon inserting objects under the rough interface, especially when these objects are penetrable.

To deal with this complex scenario, we apply the steepest descent fast multipole method (SDFMM), originally developed by Jandhyala, Michielssen, and Chew (see [1]–[3]) to analyze 3-D scattering problems of quasi-planar structures, which is well suited to handle large computational domains of this sort. In particular, the SDFMM computer code has been successfully modified to handle objects with burial depth comparable to the wavelength and varieties of ground soil characteristics. Mine fields are located in different places all over the world where the dielectric constant of the soil significantly varies, e.g., $\varepsilon_r = 2.5 - i0.18$ for Bosnian soil with 3.8% moisture at 1 GHz, $\varepsilon_r = 5.4 - i0.04$ for Puerto Rican soil with 10% moisture at 960 MHz, while $\varepsilon_r = 9.18 - i1.26$ for Bosnian soil with 25% moisture at 1 GHz. These modifications and their use in calculating scattering simulations are presented in this work. The SDFMM is a hybridization of three methods:

1) the method of moments (MOM);
2) the steepest descent path (SDP) method;
3) the fast multipole method (FMM).

The basic concept of the SDFMM is to subdivide the rough surface and the buried object scatterers into small groups; each group includes some of the moment method surface current unknowns. The interactions between these current unknowns in a

Manuscript received June 1, 2000; revised November 1, 2000. This work was supported by the Army Research Office Demining MURI Grant DAA 0-55-97-0013 and in part by the Engineering Research Centers Program of the NSF under Award EEC-9986821.

M. El-Shenawee is with the Department of Electrical Engineering, University of Arkansas, Fayetteville, AR 72701 USA (e-mail: magda@uark.edu).

C. Rappaport, E. Miller, and M. Silevitch are with the Center for Subsurface Sensing and Imaging Systems (CenSSIS), Department of Electrical and Computer Engineering, Northeastern University, Boston, MA 02115 USA (e-mail: rappaport@cr.neu.edu).

Publisher Item Identifier S 0196-2892(01)04836-7.

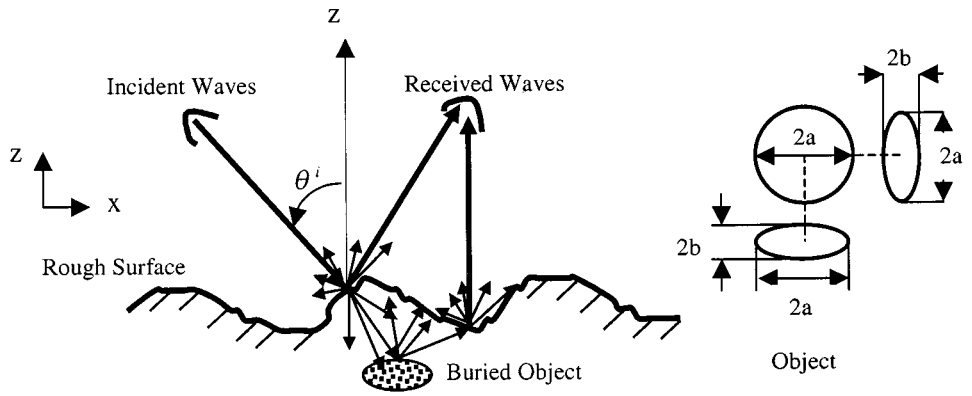


Fig. 1. Cross section of 3-D object buried under the rough surface ground. The object is modeled as oblate spheroid as: $x = a\sin(\vartheta)\cos(\phi)$, $y = a\sin(\vartheta)\sin(\phi)$, and $z = b\cos(\vartheta)$.

given group or in nearby groups are calculated using the standard MOM, which incorporates multiplying the elements of the impedance matrix by the current coefficient vector. All other interactions are calculated in one step without conducting matrix vector multiplication by using the fast multipole method, which is also hybridized with the SDP integration rule. The details of the SDFMM can be found in [1]–[6].

In Section II, we present the analysis of the problem based on extending the implementation of the PMCHW [7] integral equations for the three regions; 1) air, 2) soil, and 3) buried object. The object can either be penetrable, as characterized by its dielectric constant, or a perfect electric conductor (PEC). In Section III, the numerical results for the electric fields in the near zone are shown. Conclusions and future work will be summarized in Section IV. The proof of an important and useful identity used in the computations is given in the Appendix.

## II. Formulation

In this section, we formulate the problem of a penetrable arbitrary 3-D scatterer $R_2$ immersed in $R_1$ with an interior scatterer of different material $R_3$, as shown in Fig. 2(a). The three regions, $R_1$, $R_2$, and $R_3$ have permittivity and permeability given by $\varepsilon_1$ and $\mu_1$, $\varepsilon_2$ and $\mu_2$, and $\varepsilon_3$ and $\mu_3$, respectively. As shown in Fig. 2(a)–(d), the region $R_2$ is bounded by surfaces $S_1$ (exterior) and $S_2$ (interior) with normal vectors $\overline{n}_1$ and $\overline{n}_2$ on $S_1$ and, $\overline{n}_3$ and $\overline{n}_4$ on $S_2$. The region $R_3$ is bounded by surface $S_2$. The normal vectors $\overline{n}_1$, $\overline{n}_2$ and $\overline{n}_3$, and $\overline{n}_4$ are chosen to point toward regions $R_1$, $R_2$, and $R_3$, respectively. The electric and magnetic fields in regions $R_1$, $R_2$, and $R_3$ are $\overline{E}_1$, $\overline{H}_1$, due to equivalent currents $\overline{J}_1$, $\overline{M}_1$, as shown in Fig. 2(b), $\overline{E}_2$, $\overline{H}_2$ due to equivalent currents $\overline{J}_2$, $\overline{M}_2$ and $\overline{J}_3$, $\overline{M}_3$, as shown in Fig. 2(c), and $\overline{E}_3$, $\overline{H}_3$, due to equivalent currents $\overline{J}_4$, $\overline{M}_4$, as shown in Fig. 2(d). Following the analysis in [7], [9], and [10] with time dependence $\exp(i\omega t)$ assumed, the electric and magnetic fields at an arbitrary point $\overline{r}$ in region $R_1$ are

$$\theta_1(\overline{r})\overline{E}_1(\overline{r}) = \overline{E}^{inc}(\overline{r}) - \int_{S_1} \big(i\omega\mu_1\left(\overline{n}_1\times\overline{H}_1\right)\Phi_1 - \left(\overline{n}_1\times\overline{E}_1\right)\times\nabla'\Phi_1 - \left(\overline{n}_1\cdot\overline{E}_1\right)\nabla'\Phi_1\big)\,ds' \quad (1a)$$

$$\theta_1(\overline{r})\overline{H}_1(\overline{r}) = \overline{H}^{inc}(\overline{r}) + \int_{S_1} \big(i\omega\varepsilon_1(\overline{n}_1\times\overline{E}_1)\Phi_1 + (\overline{n}_1\times\overline{H}_1)\times\nabla'\Phi_1 + (\overline{n}_1\cdot\overline{H}_1)\nabla'\Phi_1\big)\,ds'. \quad (1b)$$

Similarly, the electric and magnetic fields in region $R_2$ are

$$\begin{aligned}\theta_2(\overline{r})\overline{E}_2(\overline{r}) = &-\int_{S_1}\big(i\omega\mu_2(\overline{n}_2\times\overline{H}_2)\Phi_2 - (\overline{n}_2\times\overline{E}_2)\times\nabla'\Phi_2 - (\overline{n}_2\cdot\overline{E}_2)\nabla'\Phi_2\big)\,ds'\\ &-\int_{S_2}\big(i\omega\mu_2(\overline{n}_3\times\overline{H}_2)\Phi_2 - (\overline{n}_3\times\overline{E}_2)\times\nabla'\Phi_2 - (\overline{n}_3\cdot\overline{E}_2)\nabla'\Phi_2\big)\,ds' \quad (1c)\end{aligned}$$

$$\begin{aligned}\theta_2(\overline{r})\overline{H}_2(\overline{r}) = &\int_{S_1}\big(i\omega\varepsilon_2(\overline{n}_2\times\overline{E}_2)\Phi_2 + (\overline{n}_2\times\overline{H}_2)\times\nabla'\Phi_2 + (\overline{n}_2\cdot\overline{H}_2)\nabla'\Phi_2\big)\,ds'\\ &+\int_{S_2}\big(i\omega\varepsilon_2(\overline{n}_3\times\overline{E}_2)\Phi_2 + (\overline{n}_3\times\overline{H}_2)\times\nabla'\Phi_2 + (\overline{n}_3\cdot\overline{H}_2)\nabla'\Phi_2\big)\,ds'. \quad (1d)\end{aligned}$$

Finally, the electric and magnetic fields in region $R_3$ are

$$\theta_3(\overline{r})\overline{E}_3(\overline{r}) = -\int_{S_2}\big(i\omega\mu_3(\overline{n}_4\times\overline{H}_3)\Phi_3 - (\overline{n}_4\times\overline{E}_3)\times\nabla'\Phi_3 - (\overline{n}_4\cdot\overline{E}_3)\nabla'\Phi_3\big)\,ds' \quad (1e)$$

$$\theta_3(\overline{r})\overline{H}_3(\overline{r}) = \int_{S_2}\big(i\omega\varepsilon_3(\overline{n}_4\times\overline{E}_3)\Phi_3 + (\overline{n}_4\times\overline{H}_3)\times\nabla'\Phi_3 + (\overline{n}_4\cdot\overline{H}_3)\nabla'\Phi_3\big)\,ds'. \quad (1f)$$

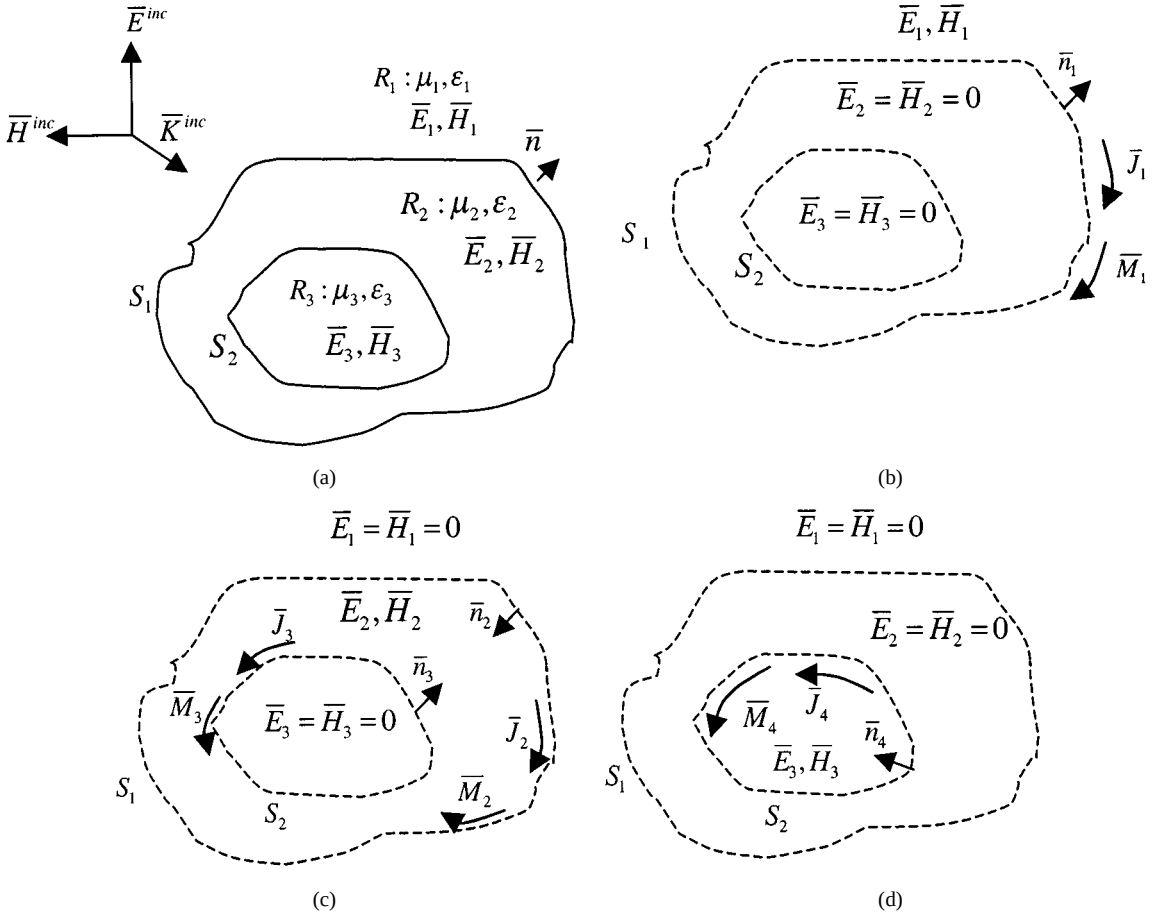


Fig. 2. (a) General penetrable 3-D scatterers $R_2$ and $R_3$. (b) Equivalent problem exterior to $S_1$. (c) Equivalent problem interior to $S_1$ and exterior to $S_2$. (d) Equivalent problem interior to $S_2$.

In (1a)–(1f), $\overline{r}$ is the field point, $\overline{r}'$ is the source point, and $\Phi_i$ is the 3-D scalar Green's function $\exp(-ik_i|\overline{r}-\overline{r}'|)/4\pi|\overline{r}-\overline{r}'|$ in which $k_i = \omega\sqrt{\varepsilon_i\mu_i}$ is the wave number in each region $i = 1, 2,$ and 3. The symbol $\theta_i(\overline{r})$ is the Heaviside function that gives the jump condition at surface $S$, [$\theta_i(\overline{r}) = 1$ for $\overline{r} \in R_i$, 0.5 for $\overline{r} \in \partial R_i$, 0 otherwise] [7], [9], [10], where the symbol $\partial R_i$ represents the boundary of region $R_i$. The equivalent currents $\overline{J}_1$ and $\overline{M}_1$ are related to the tangential electric and magnetic field components in region $R_1$ as $\overline{J}_1 = \overline{n}_1 \times \overline{H}_1|_{S_1}$ and $\overline{M}_1 = \overline{E}_1 \times \overline{n}_1|_{S_1}$. Similarly, the equivalent currents $\overline{J}_2$, $\overline{J}_3$, $\overline{J}_4$, $\overline{M}_2$, $\overline{M}_3$, and $\overline{M}_4$ can be related to tangential electric and magnetic fields on $S_1$ and $S_2$. Moreover, the normal electric and magnetic field components in region $R_1$ are related to the equivalent currents as $\overline{n}_1 \cdot \overline{E}_1 = -\nabla \cdot \overline{J}_1/i\omega\varepsilon_1$ and $\overline{n}_1 \cdot \overline{H}_1 = -\nabla \cdot \overline{M}_1/i\omega\mu_1$. Similarly, the normal electric and magnetic field components in regions $R_2$ and $R_3$ can be expressed as functions of their associated equivalent currents. Applying the boundary conditions for the tangential electric and magnetic field components on surface $S_1$ leads to $\overline{J}_1 = -\overline{J}_2$ and $\overline{M}_1 = -\overline{M}_2$, and on surface $S_2$ leads to $\overline{J}_3 = -\overline{J}_4$ and $\overline{M}_3 = -\overline{M}_4$. Thus, upon equating the tangential component of the electric fields ($\overline{E}_1$ and $\overline{E}_2$) and magnetic fields ($\overline{H}_1$ and $\overline{H}_2$), on surface $S_1$, we get

$$\overline{E}^{inc}(\overline{r})|_{\text{tang.}} = \left[(L_1 + L_2)\overline{J}_1 - (K_1 + K_2) \cdot \overline{M}_1 - L_3\overline{J}_3 + K_3\overline{M}_3\right]_{\text{tang}} \quad (2)$$

$$\overline{H}^{inc}(\overline{r})|_{\text{tang.}} = \left[(K_1 + K_2)\overline{J}_1 + \left(\frac{L_1}{\eta_1^2} + \frac{L_2}{\eta_2^2}\right) \cdot \overline{M}_1 - K_3\overline{J}_3 - \frac{L_3}{\eta_2^2}\overline{M}_3\right]_{\text{tang}} \quad (3)$$

and on surface $S_2$, we get

$$0 = \left[-L_2\overline{J}_1 + K_2\overline{M}_1 + (L_3 + L_4) \cdot \overline{J}_3 - (K_3 + K_4)\overline{M}_3\right]_{\text{tang}} \quad (4)$$

$$0 = \left[-K_2\overline{J}_1 - \frac{L_2\overline{M}_1}{\eta_2^2} + (K_3 + K_4) \cdot \overline{J}_3 + \left(\frac{L_3}{\eta_2^2} + \frac{L_4}{\eta_3^2}\right)\overline{M}_3\right]_{\text{tang}} \quad (5)$$

where, operators $L_j$ and $K_j$, $j = 1, 2, 3,$ and 4 are given by

$$L_{1,2}\overline{X} = \int_{S_1} \left\{ i\omega\mu_{1,2}\Phi_{1,2}\overline{X}(\overline{r}') + \frac{i}{\omega\varepsilon_{1,2}}\nabla\nabla' \cdot \overline{X}(\overline{r}')\Phi_{1,2} \right\} ds' \quad (6a)$$

$$L_{3,4}\overline{X} = \int_{S_2} \left\{ i\omega\mu_{2,3}\Phi_{2,3}\overline{X}(\overline{r}') + \frac{i}{\omega\varepsilon_{2,3}}\nabla\nabla' \cdot \overline{X}(\overline{r}')\Phi_{2,3} \right\} ds' \quad (6b)$$

$$K_{1,2}\overline{X} = \int_{S_1} \overline{X}(\overline{r}') \times \nabla\Phi_{1,2}\, ds' \tag{6c}$$

$$K_{3,4}\overline{X} = \int_{S_2} \overline{X}(\overline{r}') \times \nabla\Phi_{2,3}\, ds'. \tag{6d}$$

The vector $\overline{X}$ represents the surface electric current $\overline{J}$ and/or the surface magnetic current $\overline{M}$ on surface $S_1$ or on surface $S_2$. The intrinsic impedance in each region is $\eta_i = \sqrt{\mu_i/\varepsilon_i}$, where the dielectric permittivity and permeability are $\varepsilon_i$ and $\mu_i$, respectively. Equations (2)–(5) are considered the extension of the PMCHW formulation which has been shown to yield a unique solution at internal resonances associated with the corresponding conducting scatterer [7], [11], [12].

The equivalent electric and magnetic currents $\overline{J}_{1,3}$ and $\overline{M}_{1,3}$ on $S_1$ and on $S_2$, are approximated in (2)–(5) using the RWG vector basis functions $\overline{j}(\overline{r})$ [7], [8] as follows:

$$\overline{J}_1(\overline{r}) = \sum_{n=1}^{N} I_{1n}\overline{j}_{1n}(\overline{r})$$

$$\overline{M}_1(\overline{r}) = \eta_1 \sum_{n=1}^{N} I_{2n}\overline{j}_{1n}(\overline{r}), \qquad \overline{r} \in S_1 \tag{7a}$$

$$\overline{J}_3(\overline{r}) = \sum_{m=1}^{P} I_{3m}\overline{j}_{2m}(\overline{r})$$

$$\overline{M}_3(\overline{r}) = \eta_1 \sum_{m=1}^{P} I_{4m}\overline{j}_{2m}(\overline{r}), \qquad \overline{r} \in S_2 \tag{7b}$$

where $\eta_1$ is the intrinsic impedance of region $R_1$, which is the free space in this work. For the sake of computational efficiency, both magnetic currents $\overline{M}_1$ and $\overline{M}_3$ are normalized with the same value of $\eta_1$ as shown in (7a) and (7b). The number of the unknown coefficients on surface $S_1$ with coefficient vectors $I_1$ and $I_2$, which are associated with $\overline{J}_1$ and $\overline{M}_1$, is denoted by $N$, while the number of the unknown coefficients on surface $S_2$ with coefficient vectors $I_3$ and $I_4$, associated with $\overline{J}_3$ and $\overline{M}_3$, is denoted by $P$, in (7a) and (7b). Next, we substitute (7a) and (7b) in (2)–(5), along with multiplying the $H$-field equations, (3) and (5), by the same normalizing intrinsic impedance $\eta_1$. Upon applying Galerkin's method for testing the $E$- and $H$-field equations, the original integral equations are thus transformed into a set of linear equations $\overline{\overline{Z}}\overline{I} = \overline{V}$ given by

$$\begin{pmatrix} \overline{Z}_{11} & \overline{Z}_{12} \\ \overline{Z}_{21} & \overline{Z}_{22} \end{pmatrix} \begin{pmatrix} I^1 \\ I^2 \end{pmatrix} = \begin{pmatrix} \overline{V}_1 \\ 0 \end{pmatrix} \tag{8}$$

where

- $\overline{Z}_{11}$ submatrix of order $2N \times 2N$ which represents interactions between elements only on surface $S_1$;
- $\overline{Z}_{12}$ submatrix of order $2N \times 2P$ which represents interactions between elements on surface $S_1$ and elements on surface $S_2$;
- $\overline{Z}_{21}$ submatrix of order $2P \times 2N$ which represents interactions between elements on surface $S_2$ and elements on surface $S_1$;
- $\overline{Z}_{22}$ submatrix of order $2P \times 2P$ which represents interactions between elements only on surface $S_2$.

Thus, the total matrix $\overline{\overline{Z}}$ has order of $2(N+P)\times 2(N+P)$. Note that the vector $\overline{V}_1$ is a submatrix of order $2N \times 1$ and composed of the tested tangential incident electric field $\overline{E}^{inc}$ and the tested normalized magnetic field $\eta_1\overline{H}^{inc}$ on surface $S_1$. The unknown current coefficients $I^1$ and $I^2$ are submatrices of order $2N \times 1$ and $2P \times 1$. The elements of the submatrix $\overline{Z}_{11}$ are given by

$$\overline{Z}_{11} = \begin{pmatrix} \langle \overline{j}_1, (L_1+L_2)\overline{j}_1 \rangle_{S_1} & \langle \overline{j}_1, -\eta_1(K_1+K_2)\overline{j}_1 \rangle_{S_1} \\ \langle \overline{j}_1, \eta_1(K_1+K_2)\overline{j}_1 \rangle_{S_1} & \left\langle \overline{j}_1, \eta_1^2\left(\frac{L_1}{\eta_1^2}+\frac{L_2}{\eta_2^2}\right)\overline{j}_1 \right\rangle_{S_1} \end{pmatrix} \tag{9a}$$

in which $\langle \overline{A}, \overline{B} \rangle_S = \int_S \overline{A}^* \cdot \overline{B}\, ds$ denotes the complex inner product between vector functions $\overline{A}$ and $\overline{B}$ on a surface $S$ [7]. Similarly, the elements of the submatrices $\overline{Z}_{12}$, $\overline{Z}_{21}$, and $\overline{Z}_{22}$ are

$$\overline{Z}_{12} = \begin{pmatrix} \langle \overline{j}_1, -L_3\overline{j}_2 \rangle_{S_1} & \langle \overline{j}_1, \eta_1 K_3\overline{j}_2 \rangle_{S_1} \\ \langle \overline{j}_1, -\eta_1 K_3\overline{j}_2 \rangle_{S_1} & \left\langle \overline{j}_1, -\eta_1^2\left(\frac{L_3}{\eta_2^2}\right)\overline{j}_2 \right\rangle_{S_1} \end{pmatrix} \tag{9b}$$

$$\overline{Z}_{21} = \begin{pmatrix} \langle \overline{j}_2, -L_2\overline{j}_1 \rangle_{s_2} & \langle \overline{j}_2, \eta_1 K_2\overline{j}_1 \rangle_{S_2} \\ \langle \overline{j}_2, -\eta_1 K_2\overline{j}_1 \rangle_{S_2} & \left\langle \overline{j}_2, -\eta_1^2\left(\frac{L_2}{\eta_2^2}\right)\overline{j}_1 \right\rangle_{S_2} \end{pmatrix} \tag{9c}$$

$$\overline{Z}_{22} = \begin{pmatrix} \langle \overline{j}_2, (L_3+L_4)\overline{j}_2 \rangle_{S_2} & \langle \overline{j}_2, -\eta_1(K_3+K_4)\overline{j}_2 \rangle_{S_2} \\ \langle \overline{j}_2, \eta_1(K_3+K_4)\overline{j}_2 \rangle_{S_2} & \left\langle \overline{j}_2, \eta_1^2\left(\frac{L_3}{\eta_2^2}+\frac{L_4}{\eta_3^2}\right)\overline{j}_2 \right\rangle_{S_2} \end{pmatrix}. \tag{9d}$$

Notice that there are symmetrical relationships between some of the 16 submatrices in (9a)–(9d), for example, it can be proven that (see Appendix)

$$\langle \overline{j}_1, \eta_1 K_3\overline{j}_2 \rangle_{S_1} = -\langle \overline{j}_2, -\eta_1 K_2\overline{j}_1 \rangle_{S_2}. \tag{10}$$

This leads to computing and storing elements of only nine out of the above 16 submatrices, to gain significant reduction in CPU time and computer memory requirements for the MOM part.

To obtain the formulations for a PEC interior scatterer $S_2$, we delete $P$ rows and $P$ columns from the total matrix $\overline{\overline{Z}}$ starting from index $(2N+P+1)$ up to index $(2N+2P)$. Moreover, $P$ rows should be deleted from vectors $\overline{I}$ and $\overline{V}$ starting from index $(2N+P+1)$ up to index $(2N+2P)$. This leads to a new matrix $\overline{\overline{Z}}$ that has an order of $(2N+P)\times(2N+P)$.

The objective of the above analysis is to solve (8) for the unknown current coefficients $I^1$ and $I^2$. Upon substituting the obtained coefficients into (7a) and (7b), the surface electric and magnetic currents can be obtained on the exterior scatterer $S_1$ and on the interior scatterer $S_2$. Thus, complex vector electric fields in the near zone can be obtained [13].

As is well known, solving the system of equations in (8) by using the MOM requires computing, storing and multiplying a full dense matrix of order $2(N+P)\times 2(N+P)$ by a vector of order $2(N+P)$, which is computationally prohibitive for large-scale scatterers even using supercomputers. This necessitates the need for the SDFMM, which makes these computations significantly tractable. Applying the SDFMM to (8), the matrix $\overline{\overline{Z}}$ is divided as $\overline{\overline{Z}}^{NF}+\overline{\overline{Z}}^{FF}$, where $\overline{\overline{Z}}^{NF}$ represents the dense near field part, and $\overline{\overline{Z}}^{FF}$ represents the sparse far field part of matrix $\overline{\overline{Z}}$. The entries of $\overline{\overline{Z}}^{NF}$ are computed directly, and then the matrix vector multiply is conducted following the conventional MOM method. The entries of $\overline{\overline{Z}}^{FF}$ are not directly computed nor stored as before, but the matrix vector multiply is conducted in one step using the inhomogeneous plane wave expansions. The interaction decomposition into near field $NF$ and far field $FF$ is assumed according to the distance, in wavelength, between those interacting elements on the scatterer. We should mention that the computational complexity of the SDFMM for the CPU time and the memory requirement are of $O(K)$ per iteration of the iterative solver, while they are of order $O(K^2)$ for the MOM method, where $K$ is the total number of the surface current unknowns and it is equal to $2(N+P)$ for the buried penetrable object case [1]–[6].

## III. Numerical Results

In this work, the exterior closed scatterer $S_1$ is excited with an incident Gaussian beam that induces stronger surface currents on a localized area of the surface and weaker currents away from that area [14], [15]. As a result, these surface currents become negligible on the back of the closed surface $S_1$, which makes it possible to approximate $S_1$ by an open rough surface with dimensions $L\times L$. In all results here, $L$ is chosen to be $8\lambda_0$ where $\lambda_0$ is the free-space wavelength. In reality, the rough surface is an infinite surface, but by using a carefully tapered incident Gaussian beam, the edge effect of the modeled finite surface can be eliminated. The random rough surface, characterized by Gaussian statistics for the random heights and for the autocorrelation function, is generated using the computer random number generator [16] and will be described by the root mean square height $\sigma$ and the correlation length $l_c$. The interior scatterer $S_2$ is representing the object, which is always buried at the center of the ground with burial depth measured from its center to the mean plane of the rough surface.

In Fig. 3(a) and (b), the SDFMM computer code is compared with the sparse matrix canonical grid (SMCG) method published in [14]. The buried object is assumed to be a PEC sphere of radius $r=0.3\lambda_0$ at burial depth $d=0.6\lambda_0$, where the incident angle is $\vartheta^i=20°$ and the relative dielectric constant of the soil is $\varepsilon_r=2.0-i0.2$. The HH-polarization results for the normalized radar cross section (RCS) is shown for the rough surface ($\sigma=0.02\lambda_0$ and $l_c=0.5\lambda_0$) without the buried PEC sphere in Fig. 3(a) and with the buried PEC sphere in Fig. 3(b). The horizontal axis in Fig. 3 is the scatter angle $\theta$ (elevation angle in degrees) measured from the $z$-axis. For comparison purposes with [14], the rough surface is sampled at eight points per $\lambda_0$ leading to a number of surface current unknowns $N=12\,160$

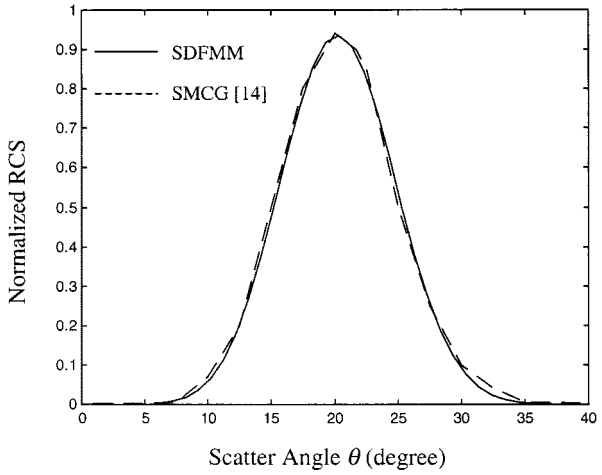


(a)

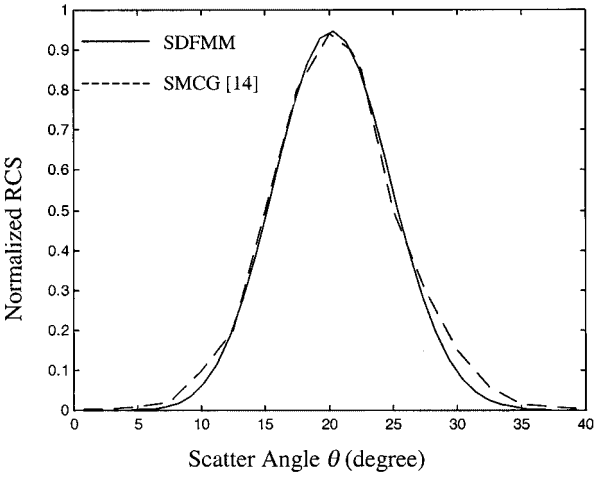


(b)

Fig. 3. (a) Normalized RCS for rough surface of root mean square height $\sigma=0.02\lambda_0$ and correlation length $l_c=0.5\lambda_0$, at incident angle $\vartheta^i=20°$. HH-polarization. (b) Normalized RCS for a PEC sphere buried under rough surface of root mean square height $\sigma=0.02\lambda_0$ and correlation length $l_c=0.5\lambda_0$, with burial depth (from the center) $d=0.6\lambda_0$, and sphere radius $r=0.3\lambda_0$ at incident angle $\vartheta^i=20°$. HH-polarization.

as in [14]. The PEC sphere is sampled at 20 points in the $\phi$-direction 0–360° and 10 points in the $\vartheta$-direction 0–90° leading to a number of surface current unknowns $P=480$. The normalized RCS is calculated by taking the average of those values produced using ten azimuth angles. The excellent agreement shown in these figures validates the SDFMM code for the buried PEC object under the rough ground.

Next, new analysis of a buried penetrable or PEC oblate spheroid of dimensions $a=0.3\lambda_0$ and $b=0.15\lambda_0$, as shown in Fig. 1, is presented. To assure accuracy, the rough surface is sampled at 12.5 points per $\lambda_0$ with a number of surface current unknowns equal to $N=29\,800$. The spheroid is sampled at 20 points in the $\phi$-direction and eight points in the $\vartheta$-direction corresponding to $P=360$ surface current unknowns.

In Fig. 4(a)–(d), the magnitude of the complex vector electric field in the near zone is calculated at height $z=0.5\lambda_0$ above and below the nominal ground and at $(x, y)$ grid points of resolution equal to $0.1\lambda_0$. The ground surface is rough with $\sigma=0.04\lambda_0$, $l_c=0.5\lambda_0$, and relative dielectric constant $\varepsilon_r=2.5-i0.18$

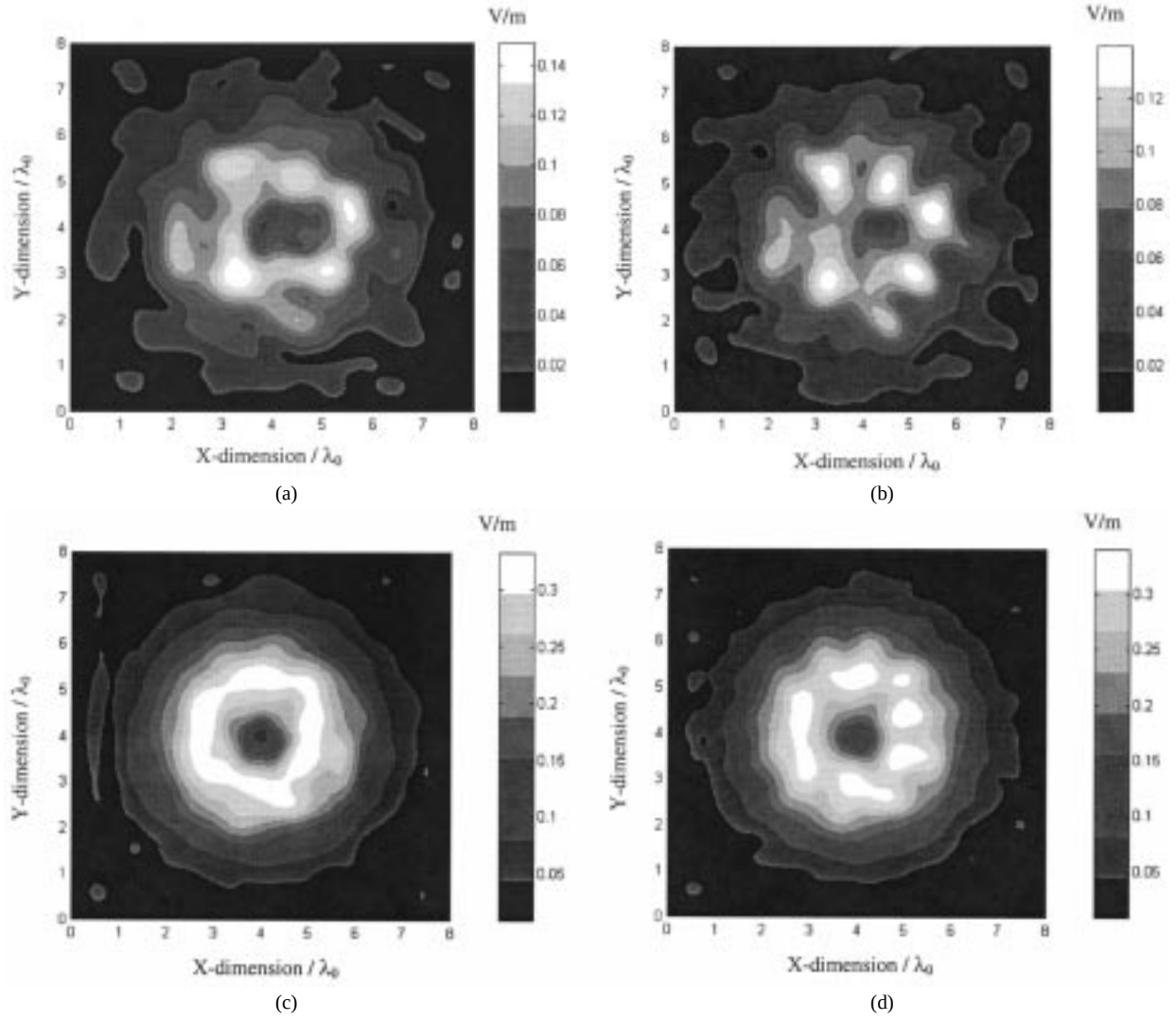


Fig. 4. (a) Near scattered electric field at $z = 0.5\lambda_0$ for H-incident polarization from rough surface of root mean square height $\sigma = 0.04\lambda_0$ and correlation length $l_c = 0.5\lambda_0$, at incident angle $\vartheta^i = 10°$. (b) Near scattered electric field at $z = 0.5\lambda_0$ for V-incident polarization from rough surface of root mean square height $\sigma = 0.04\lambda_0$ and correlation length $l_c = 0.5\lambda_0$, at incident angle $\vartheta^i = 10°$. (c) Near transmitted electric field at $z = -0.5\lambda_0$ for H-incident polarization from rough surface of root mean square height $\sigma = 0.04\lambda_0$ and correlation length $l_c = 0.5\lambda_0$, at incident angle $\vartheta^i = 10°$. (d) Near transmitted electric field at $z = -0.5\lambda_0$ for V-incident polarization from rough surface of root mean square height $\sigma = 0.04\lambda_0$ and correlation length $l_c = 0.5\lambda_0$, at incident angle $\vartheta^i = 10°$.

which is a typical Bosnian dry (3.8% moisture) clay loam at 1 GHz [17]. To enhance target detection, the near scattered electric field is computed and averaged over multiple views each pointed to the same ground point directly over the target. Ten incident Gaussian beams with same elevation angle $\vartheta^i = 10°$ and different azimuth angles $\phi^i = 0,\ 36,\ 72,\ \ldots 324°$, are simulated as suggested by Zhang *et al.* [14]. The rational of averaging over these multiple views is that this process minimizes the clutter effect of the rough surface on individual scattered beams. In Fig. 4(a) and (b), the magnitude of the near electric field scattered from the rough surface only is plotted for the H- and V-incident polarization, respectively, while in Fig. 4(c) and (d), the near electric field transmitted into the same rough ground is plotted for the H- and V-polarizations, respectively. The shown results in Fig. 4(a) and (b) indicate the difference in the scattered electric fields upon changing the polarization of the incident Gaussian beam (H and V). Notice that in the H-polarization at oblique incident angle $\vartheta^i = 10°$, the incident electric field always has a single component perpendicular to the plane of incidence ($y$-component for $\phi^i = 0,\ \pi$), while it has two components ($x$- and $z$- for $\phi^i = 0,\ \pi$) in the V-polarization. Accordingly, the local reflection and transmission coefficients on each point on the rough surface are different, giving rise to the difference observed between Fig. 4(a) and (b) and between Fig. 4(c) and (d). As seen in Fig. 4(a) and (b), the scattered electric fields for each polarization appear to have ten lobes, one every 36° in azimuth direction (as seen clearly at the 0.062 V/m contour level). For a perfectly flat surface, the scattered pattern would have tenfold symmetry, but for the rough surface, the random variations distort this pattern. As expected, the transmitted electric fields shown in Fig. 4(c) and (d) are larger than the scattered electric fields shown in Fig. 4(a) and (b) due to the relatively small value of the dielectric constant $(\varepsilon_r = 2.5 - i0.18)$. Moreover, the results show that the electric fields transmitted into the ground are less distorted than the scattered electric fields. This is because the local transmitted angle is smaller than the local incident angle.

The near electric field scattered from the oblate PEC spheroid buried at depth $d = 0.3\lambda_o$ is calculated for the H- and V-incident polarizations. The results obtained are only slightly different from those presented in Fig. 4(a) and (b), therefore they are not presented here. The near electric field scattered due just to the object, obtained by subtracting the electric fields scattered from the surface only [Fig. 4(a) and (b)] from the electric fields scattered from the surface with the buried object, is shown in Fig. 5(a) and (b) for H- and V-polarization, respectively. The results indicate that the signature of the buried oblate PEC spheroid is smaller than the ground scattered field, since the target is small compared with the wavelength, and is a polarization dependent, as expected, with almost four times larger magnitude V-polarization than H-polarization.

The oblate penetrable spheroid with the relative dielectric constant of TNT $\varepsilon_r = 2.9 - i0.07$, is buried under the same rough surface as before at the same depth $d = 0.3\lambda_0$. The near electric scattered fields due just to the oblate penetrable spheroid are shown in Fig. 6(a) and (b) for H- and V-polarization, respectively. These results indicate that the signature of the oblate penetrable spheroid is not as polarization dependent as that of the oblate PEC spheroid shown in Fig. 5(a) and (b). Since the Gaussian beams on opposite sides of the object are oppositely polarized, electric fields scattered from the centered object tend to cancel. It is interestingly to note that the rough ground surface perturbs this destructive interference. The average scattered electric field from the PEC object illuminated by V-polarized beams [Fig. 5(b)] is greater than for the H-polarized beams [Fig. 5(a)], due to constructive interference of the $z$-components. If a progressive phase of $2\pi/10$ is successively applied to each of the scattered electric fields to focus the field at the center, stronger but almost equal signatures of the PEC object are observed in both polarizations providing a stronger but less discriminative detecting technique.

The iterative solver TFQMR [18] has been used with tolerance 1% for all obtained results. Five levels in the fast multilevel multipole part of the SDFMM with finest block size equal to $0.5025\lambda_0$ were employed here. For the oblate penetrable spheroid case, the SDFMM code needed 2 CPU h, using one processor on Compaq GS140 EV6 machine, for the iterative solver to converge for each incident beam and additional 35 min for the set-up time. Thus the total required CPU time, for ten multiple views, is 20.6 CPU h. The required computer memory is 800 MB. For the oblate PEC buried spheroid, the SDFMM code needed 1.6 CPU h per view for the iterative solver and almost the same set-up time as before leading to total time of 16.5 CPU h in this case. The required computer memory in later case was 600 MB. For the rough surface only, the SDFMM code needed 0.9 CPU h for the iterative solver, 30 min for set-up time, and 500 MB computer memory.

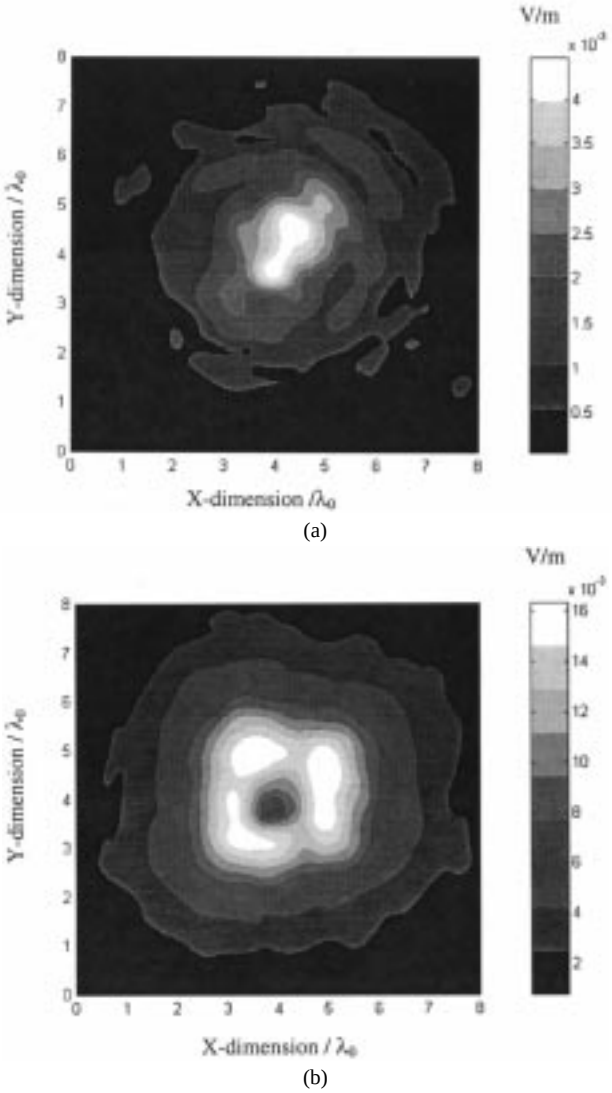


Fig. 5. (a) Near scattered electric field at $z = 0.5\lambda_0$ for H-incident polarization due only to the PEC spheroid (obtained by subtraction). (b) Near scattered electric field at $z = 0.5\lambda_0$ for V-incident polarization due only to the PEC spheroid (obtained by subtraction).

## IV. Conclusions

In this paper, a study has been presented for 3-D electromagnetic scattering from shallow objects buried under the random rough surface. Our analysis in not limited to any particular incident waves, transmitter position, near or far field zone, object's geometry, nor to the Gaussian statistics characterization of the rough surface. There is a limitation, however, on the rough surface root mean square height and on the burial depth of the object due to the constraint of the SDFMM to quasi-planar structures. In the current application, this is not a major limitation since the surface root mean square height and the burial depth of the object are comparable to the free-space wavelength as a typical case for antipersonnel mine detection application. The ultimate objective of our research is to distinguish between the target signal scattered from the buried object and the clutter signal scattered from the rough ground. As our numerical results show, only a slight difference can be observed between these two signals because of the small size and dielectric contrast of the buried target with respect to the surrounding soil. Even though subtracting the two signals could clearly lead to the target signal, it is not a practical detection method. With the insight gained from the numerical simulations, we aim to derive methods to remove the clutter signal to achieve target detection with minimum "false alarms." Ongoing research using these numerical simulations tests advanced and robust signal processing techniques and provides a basis to

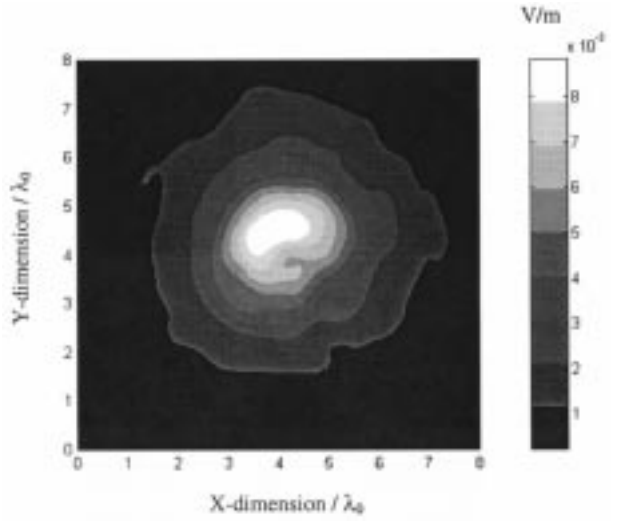


(a)

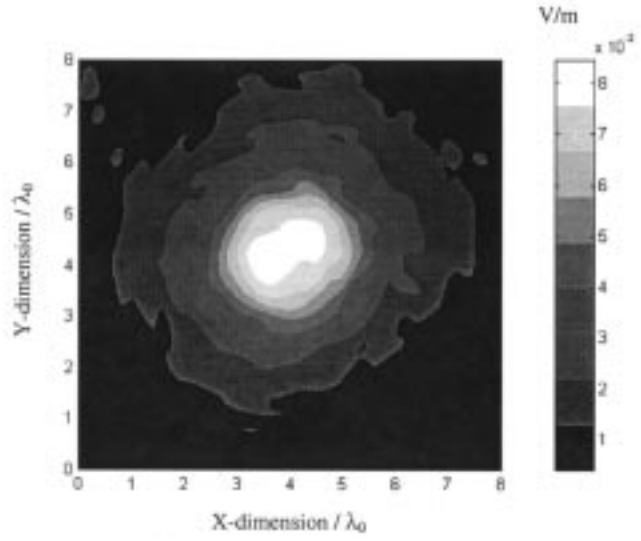


(b)

Fig. 6. (a) Near scattered electric field at $z = 0.5\lambda_0$ for H-incident polarization due only to the penetrable spheroid (obtained by subtraction). (b) Near scattered electric field at $z = 0.5\lambda_0$ for V-incident polarization due only to the penetrable spheroid (obtained by subtraction).

optimize transmitter/receiver positions for best target detection. Interestingly, our results show that the scattered electric fields above the ground undergoes strong distortion compared with the electric fields transmitted into the ground. Moreover, employing multiple views of the target using ten simultaneous incident Gaussian beams has lead to strong polarization dependency only for the PEC object, which can be used in target discrimination.

## APPENDIX

The LHS of (10) can be written as

$$\begin{aligned}\left\langle \bar{j}_1,\, \eta_1 K_3 \bar{j}_2 \right\rangle_{S_1} &= \eta_1 \int_{S_1} \bar{j}_1(\bar{r}) \\ &\quad \cdot \left( \int_{S_2} \bar{j}_2(\bar{r}') \times \nabla \Phi_2 \left( |\bar{r} - \bar{r}'| \right) ds' \right) ds \\ &= -\eta_1 \int_{S_1} \int_{S_2} \bar{j}_2(\bar{r}) \\ &\quad \cdot \left( \bar{j}_1(\bar{r}') \times \nabla \Phi_2 \left( |\bar{r} - \bar{r}'| \right) \right) ds'\, ds \quad \text{(A1)}\end{aligned}$$

where $\bar{r}'$ is the vector position on $S_2$ and $\bar{r}$ is the vector position on $S_1$. From the RHS of (10), with using $\nabla \Phi = -\nabla' \Phi$, we get

$$\begin{aligned}-\left\langle \bar{j}_2,\, -\eta_1 K_2 \bar{j}_1 \right\rangle_{S_2} &= \eta_1 \int_{S_2} \bar{j}_2(\bar{r}) \\ &\quad \cdot \left( \int_{S_1} \bar{j}_1(\bar{r}') \times \nabla \Phi_2 \left( |\bar{r} - \bar{r}'| \right) ds' \right) ds \\ &= -\eta_1 \int_{S_2} \int_{S_1} \bar{j}_2(\bar{r}) \\ &\quad \cdot \left( \bar{j}_1(\bar{r}') \times \nabla' \Phi_2 \left( |\bar{r} - \bar{r}'| \right) \right) ds'\, ds \quad \text{(A2)}\end{aligned}$$

where $\bar{r}'$ is the vector position on $S_1$ and $\bar{r}$ is the vector position on $S_2$. Upon renaming $\bar{r}'$ by $\bar{r}$, and vice versa, and exchanging the order of integrations in (A2), we get

$$\begin{aligned}-\left\langle \bar{j}_2,\, -\eta_1 K_2 \bar{j}_1 \right\rangle_{S_2} &= -\eta_1 \int_{S_2} \int_{S_1} \bar{j}_2(\bar{r}') \\ &\quad \cdot \left( \bar{j}_1(\bar{r}) \times \nabla \Phi_2 \left( |\bar{r} - \bar{r}'| \right) \right) ds\, ds' \\ &= -\eta_1 \int_{S_1} \int_{S_2} \bar{j}_2(\bar{r}') \\ &\quad \cdot \left( \bar{j}_1(\bar{r}) \times \nabla \Phi_2 \left( |\bar{r} - \bar{r}'| \right) \right) ds'\, ds. \quad \text{(A3)}\end{aligned}$$

Notice that (A3) is equivalent to (A1), which proves (10). Thus, the only nine submatrices computed and stored here are: three submatrices in $\overline{\overline{Z}}_{11}$, three submatrices in $\overline{\overline{Z}}_{22}$, two submatrices in $\overline{\overline{Z}}_{12}$, and one submatrix in $\overline{\overline{Z}}_{21}$.

## ACKNOWLEDGMENT

The authors would like to thank Prof. W. Chew and Prof. E. Michielssen at UIUC for allowing them the use and modification of the SDFMM computer code for the current application. This work benefited from the allocation of time at the Northeastern University Advanced Scientific Computation Center (NU-ASCC).

## REFERENCES

[1] V. Jandhyala, "Fast multilevel algorithms for the efficient electromagnetic analysis of quasi-planar structures," Ph.D. dissertation, Dept. Elect. Comput. Eng., Univ. Illinois, Urbana, 1998.

[2] V. Jandhyala, E. Michielssen, B. Shanker, and W. C. Chew, "A combined steepest descent-fast multipole algorithm for the fast analysis of three-dimensional scattering by rough surfaces," *IEEE Trans. Geosci. Remote Sensing*, vol. 36, pp. 738–748, May 1998.

[3] V. Jandhyala, B. Shanker, E. Michielssen, and W. C. Chew, "A fast algorithm for the analysis of scattering by dielectric rough surfaces," *J. Opt. Soc. Amer. A, Opt. Image Sci.*, vol. 15, pp. 1877–1885, July 1998.

[4] M. El-Shenawee, V. Jandhyala, E. Michielssen, and W. C. Chew, "An enhanced steepest descent fast multipole method for the analysis of scattering from two dimensional multilayered rough surfaces," in *Proc. IEEE Antennas and Propagation Soc./URSI*, Atlanta, GA, June 1998, p. 182.

[5] ——, "The steepest descent fast multipole method (SDFMM) for solving combined field integral equation pertinent to rough surface scattering," in *Proc. IEEE Antennas and Propagation Soc./URSI*, 1999, pp. 534–537.
[6] W. C. Chew, M. El-Shenawee, V. Jandhyala, and E. Michielssen, "Scattering at low grazing angels from large scale two dimensional random rough surfaces using the steepest descent fast multipole method (SDFMM)," in *Proc. 26th General Assembly*, 1999, p. 195.
[7] L. Medgyesi-Mitschang, J. Putnam, and M. Gedera, "Generalized method of moments for three-dimensional penetrable scatterers," *J. Opt. Soc. Amer. A*, vol. 11, pp. 1383–1398, Apr. 1994.
[8] S. M. Rao, D. R. Wilton, and A. W. Glisson, "Electromagnetic scattering by surfaces of arbitrary shape," *IEEE Trans. Antennas Propagat.*, vol. AP-30, pp. 409–418, May 1982.
[9] A. Poggio and E. Miller, "Integral equation solutions of three-dimensional scattering problems," in *Computer Techniques for Electromagnetics*, 2nd ed, R. Mittra, Ed. New York: Hemisphere, 1987, pp. 159–264.
[10] J. Stratton, *Electromagnetic Theory*. New York: McGraw-Hill, ch. 8, pp. 434–481.
[11] J. R. Mautz and R. F. Harrington, "H-field, E-field, and combined field solutions for conducting bodies of revolutions," *Arch. Elek. Ubertrang.*, vol. 32, pp. 157–164, 1978.
[12] P. L. Huddleston, L. N. Medgyesi-Mitschang, and J. M. Putnam, "Combined field integral equation formulation for scattering from dielectrically coated conducting bodies," *IEEE Trans. Antennas Propagat.*, vol. AP-34, pp. 510–520, 1986.
[13] C. A. Balanis, *Advanced Engineering Electromagnetics*. New York: Wiley, ch. 6, pp. 254–309.
[14] G. Zhang, L. Tsang, and K. Pak, "Angular correlation function and scattering coefficient of electromagnetic waves scattered by a buried object under a two-dimensional rough surface," *J. Opt. Soc. Amer. A*, pp. 2995–3002, Dec. 1998.
[15] P. Tran and A. A. Maradudin, "Scattering of a scalar beam from a two-dimensional randomly rough hard wall: Enhanced backscatter," *Phy. Rev. B*, vol. 45, no. 7, pp. 3936–3939, Feb. 1992.
[16] N. Garcia and E. Stoll, "Monte Carlo calculation for electromagnetic-wave scattering from random rough surfaces," *Phy. Rev. Lett.*, vol. 52, no. 20, pp. 1798–1801, May 1984.
[17] J. Curtis, "Dielectric properties of soils; various sites in Bosnia," U.S. Army Corp. Eng., Waterways Experiment, Station Data Rep., 1996.
[18] R. W. Freund, "A Transpose-free quasi-minimal residual algorithm for non-Hermitian linear systems," *SIAM J. Sci. Comput.*, vol. 14, pp. 470–482, Mar. 1993.

**Magda El-Shenawee** (M'91) received the B.S. and M.S. degrees in electrical engineering from Assiut University, Assiut, Egypt, and the Ph.D. degree in electrical engineering from the University of Nebraska, Lincoln, in 1991.

In 1992, she worked as a Research Associate in the Center for Electro-Optics at the University of Nebraska, where she focused on the problem of enhanced backscatter phenomena. In 1994, she was a Research Associate at the National Research Center, Cairo, Egypt, and in 1997, she was a Visiting Scholar at the University of Illinois at Urbana-Champaign. In 1999, she joined the MURI team (Multidisciplinary University Research Initiative) at Northeastern University, Boston, MA. Currently, she is an Assistant Professor in the Department of Electrical Engineering at the University of Arkansas, Fayetteville. Her research areas are rough surface scattering, computational electromagnetics, subsurface sensing of buried objects, numerical methods, and microstrip circuits.

Dr. El-Shenawee is a Member of the Eta Kappa Nu Electrical Engineering Honor Society.

**Carey M. Rappaport** (S'80–M'87–SM'96) received the S.B. degree in mathematics, the S.B., S.M., and E.E. degrees in electrical engineering in June 1982, and the Ph.D. degree in electrical engineering in June 1987, all from the Massachusetts Institute of Technology (MIT), Cambridge.

He has worked as a Teaching and Research Assistant at MIT from 1981 to 1987, and during the summers at COMSAT Labs, Clarksburg, MD, and The Aerospace Corporation, El Segundo, CA. He joined the faculty at Northeastern University, Boston, MA, in 1987. He has been Professor of Electrical and Computer Engineering since July 2000. During Fall 1995, he was Visiting Professor of Electrical Engineering at the Electromagnetics Institute of the Technical University of Denmark, Lyngby, as part of the W. Fulbright International Scholar Program. He has consulted for Geo-Centers, Inc., PPG, Inc., and several municipalities on wave propagation and modeling, and microwave heating and safety. He is Principal Investigator of the ARO Multidisciplinary University Research Initiative in Humanitarian Demining and Co-Principal Investigator of the Center for Subsurface Sensing and Imaging Systems (CenSSIS) Engineering Research Center. He has authored over 180 technical journal and conference papers in the areas of microwave antenna design, electromagnetic scattering computation, and bioelectromagnetics, and has received two reflector antenna patents, two biomedical device patents, and three subsurface sensing device patents.

Prof. Rappaport was awarded the IEEE Antenna and Propagation Society's H. A. Wheeler Award for Best Applications Paper of 1985. He is a Member of Sigma Xi and Eta Kappa Nu.

**Eric L. Miller** (S'90–M'95) received the S.B. degree in 1990, the S.M. degree in 1992, and the Ph.D. degree in 1994, all in electrical engineering and computer science from the Massachusetts Institute of Technology (MIT), Cambridge.

He is currently an Associate Professor in the Department of Electrical and Computer Engineering at Northeastern University, Boston, MA. His research interests include the use of multiscale and statistical methods for the solution of inverse problems in general and inverse scattering problems in particular, and the development of computationally efficient, physically-based models for use in applications such as mine detection, target recognition, medical imaging, and environmental monitoring and remediation.

Dr. Miller is a member of Tau Beta Pi, Eta Kappa Nu, and Phi Beta Kappa and received the CAREER Award from the National Science Foundation in 1996. He is currently serving as an Associate Editor for the IEEE TRANSACTIONS ON IMAGE PROCESSING.

**Michael B. Silevitch** was born in 1942. He received the Ph.D. degree in electrical engineering from Northeastern University, Boston, MA, in 1970.

Currently, he is a Professor of Electrical and Computer Engineering at Northeastern University. He is also the Director of the Center for Subsurface Sensing and Imaging Systems (CenSSIS), a newly designated NSF Engineering Research Center (ERC). His research interests include electromagnetic wave propagation, statistical mechanics, and plasma dynamics with application to the aurora borealis and other space plasmas. Since 1988, he has had a strong involvement in the development of K–12 education initiatives focusing upon the implementation of standards-based science and mathematics curricula. He is the founder of two NSF Industry-University Centers—The Center for Electromagnetics Research (CER) and the Center for the Enhancement of Science and Mathematics Education (CESAME).